WILEY

Research Article

Characteristic Analysis and Modeling of Train-to-Train Wireless Channel in Station Scenario

Yingfei Liu [1,2] **Lei Xiong**, [1] **Dan Fei**, [1] **Rui Liu**, [2] and **Endale Legesse Habte** [2]

[1]*The State Key Laboratory of Advanced Rail Autonomous Operation, Beijing Jiaotong University, Beijing 100044, China*
[2]*School of Electronic and Information Engineering, Beijing Jiaotong University, Beijing 100044, China*

Correspondence should be addressed to Lei Xiong; lxiong@bjtu.edu.cn

In this paper, ray tracing (RT) is used to analyze the characteristics of train-to-train (T2T) wireless channel in 2.1 GHz frequency band, including path loss, multipath clustering, delay spread, Rice factor, angular spread, and channel nonstationarity. It is found that the change of environment has a great influence on the characteristics of the wireless channel, which not only causes the birth and death of multipath clusters but also makes the channel appear nonstationary characteristics. In order to characterize the nonstationarity of the T2T wireless channel, we introduce the time correlation coefficient (TPCC) of the power delay profile (PDP), analyze the nonstationarity of the T2T wireless channel, and give the quasi-stationarity distance. The results are basically consistent with the measured data.

1. Introduction

With the development of the next-generation train control system, T2T communication has gradually become the focus of academic research in order to ensure the real time and accuracy of the high-speed railway mobile communication system. T2T can assist the train operation control system based on train-to-ground (T2G) wireless communication, reduce communication delay, strengthen collision danger detection and broadcast warning, and improve train operation efficiency and safety. At the same time, T2T is also a key technology for virtual coupling and autonomous driving.

So far, the international academic research on radio wave propagation and wireless channel characteristics in railway scenarios has basically focused on the T2G wireless channel. For example, the channel models of tunnel [1–3], plain [4], viaduct [3, 5, 6], cutting [7, 8], and bridge crossing scenes [9] are established. However, the research on the T2T wireless channel is relatively few. Compared with T2I communication, T2T communication presents high dynamic characteristics of both receiver and transmitter. The rapid change of environment and scatterers in a short time makes the channel characteristics change dramatically. The T2T channel is not only fast time-varying but also nonstationary.

Given that the multiple-input multiple-output (MIMO) technology can effectively improve the channel capacity and channel reliability, and the large surface area of the train car is easy to install the MIMO antenna system, it is possible to combine the MIMO technology with the channel spatial characterization study of T2T. A large-scale MIMO channel measurement campaign was conducted in an indoor metro environment at 3.5 GHz carrier frequency and 160 MHz bandwidth by Asad Saleem et al. The channel parameters were investigated for both copolarization and cross-polarization. The results show that the antenna configuration and polarization type have a large impact on the channel characteristics. The angular extension changes significantly when different antenna polarizations are used on the transmitter and receiver antenna sides [10]. Asad Saleem et al. investigated the statistical properties of a novel geometry-based three-dimensional (3D) stochastic model for next-generation vehicle-to-vehicle (V2V) multiple-input multiple-output (MIMO) communications in a nonisotropic scattering environment [11].

The Roll2Rail project established by the European Union in Shift2Rail is already conducting T2T wireless channel research. Unterhuber et al. conducted a measurement campaign on a T2T channel traveling on two parallel tracks in an open-field environment. The GSCM based on delay, Doppler frequency, and power output was compared with measurements in equivalent environments and scenarios. Finally, the model was qualitatively validated based on PDP and DSD and found to be in good agreement between the model and the measured data [12]. A train-to-train millimeter-wave propagation measurement campaign in the service of virtual coupling was carried out by Soliman et al. The received signal power in the open area was analyzed and modeled using a two-ray path loss model. The results show that the received power near the platform is higher than in the open area due to the strong contribution of the reflected signal from the platform [13]. Bignôtte et al. presented six tapped delay line models for T2T communication. The hilly terrain and train station scenarios cover large, medium, and short distances. The results show that simulated channels using any of the proposed models correlate with measurements made using a DLR channel sounder. The proposed TDL model can be modeled, and the maximum number of taps is equal to 16 [14]. Unterhuber and Walter et al. extracted channel parameters for train-to-train scenarios for typical environments such as train stations, open fields, and hilly terrain. Smoothness of the channel in time and frequency is dealt with, and distance-dependent model parameters are proposed for all random channel parameters [15]. The Briso-Rodríguez et al. conducted T2T channel measurements and modeling in the 900 MHz and 2400 MHz frequency bands of the Madrid Metro tunnel scenarios [16]. It is found that for straight tunnels, the path loss factor n is 1.139 (900 MHz band) and 1.071 (2400 MHz band), respectively, and for curved tunnels, the path loss model is a piecewise function. Ke Guan from Beijing Jiaotong University and others developed channel measurement equipment based on UWB (ultra-wideband) technology, conducted channel measurements on the terahertz frequency band T2T channel, extracted channel characteristics, and physically explained the channel characteristics using self-developed RT technology [17].

Most of the existing literature is about channel measurements for scenarios such as highways, cities, and suburbs, which involve communication between two vehicles. For high-speed railway scenarios, the cost of channel measurements is high and the feasibility of implementation is low, and few of the existing studies have investigated the channel of T2T. Therefore, in this paper, we adopt the RT technique, which is less costly, less time-consuming, and easier to implement, to establish a three-dimensional radio wave propagation scenario model to analyze and study the radio wave propagation and channel characteristics of T2T. Due to the high-speed movement of the double ends of the train, the changes in the scenario within a short period of time will cause drastic changes in the channel characteristics and the challenge of channel nonstationary brought by T2T communication needs to be paid more attention to.

Meanwhile, in T2T scenarios, the collection of scatterers in the surrounding makes the multipath signals arrive in the form of clusters; however, due to the rapid change of scatterers in the environment, significant multipath birth and death phenomena will occur. Studying the environmental factors affecting the multipath components and clustering the MPCs to further investigate the multipath cluster birth and death process can more accurately reflect the propagation of the signal in the environment and establish the channel model. Therefore, it is necessary to analyze the characteristics of the T2T wireless channel, which lays a foundation for the design of the communication system and train control system.

The station is an important scenario of high-speed railway and also a very complex scenario of radio wave propagation. Therefore, this paper mainly focuses on the station communication scenario and uses the RT technology to analyze the radio wave propagation mechanism and wireless channel characteristics between high-speed trains under the target frequency band of 5 G-R selected by the China National Railway Group (2.1 GHz). The time-varying nonstationary characteristics and dynamic multipath clustering characteristics of the T2T wireless channel are emphatically studied, and the time-varying nonstationary channel model is established, and it provides reference for T2T communication system optimization.

The rest of the paper is arranged as follows: in Section 2, 3D modeling of high-speed train and station scenarios is discussed and the ray-tracing technology and the parameters of simulation configuration are introduced; in Section 3, the channel data obtained from RT simulation are processed, the channel characteristics are extracted, and the multipath clustering and time-varying nonstationary characteristics are analyzed and modeled; Section 4 summarizes channel characteristics and gives recommendations.

2. Three-Dimensional Scenario Modeling

2.1. The Train Model. According to CRH380AL train, the high-speed train model is established. CRH380AL train adopts 8-section and 16-section marshalling. In order to reduce the complexity of the model and the operational difficulty of the simulation without affecting the simulation results, the 8-section marshalling train model is established in this paper, as shown in Figure 1. The train is 201.50 m long, 3.38 m wide, and 3.70 m high.

2.2. Scenario Models. This paper refers to Tianmen North Station in Hubei Province for station scenario modeling. The station has a scale of 2 sets and 6 tracks (2 main tracks and 4 arrival and departure tracks), the effective length of the arrival and departure tracks is 650 m, and there are 2 middle island platforms of 450 m × 12 m × 1.25 m. The platform houses and platforms are arranged in equal length, among which tracks 1, 2, 5, and 6 are arrival and departure tracks and tracks 3 and 4 are main tracks. The 3D model diagram of the station scenario is shown in Figure 2.
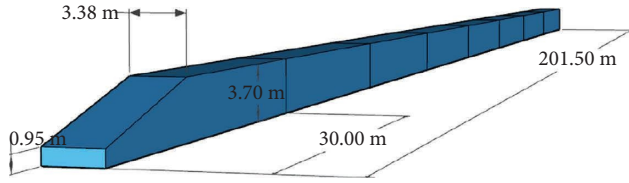
FIGURE 1: Train model: the black mark represents the size data of the train.
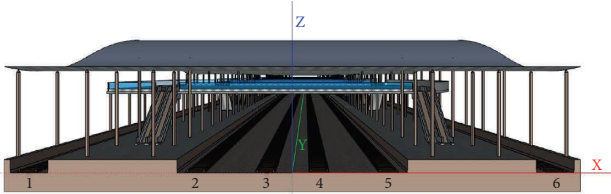

FIGURE 2: Station scenario model: the graphical annotations include the selection of axes and the distribution of each track.

In the station scenario, take the track direction as the y-axis (green coordinate axis), the horizontal plane perpendicular to the track direction as the x-axis (red coordinate axis), and the vertical plane to the ground direction as the z-axis (blue coordinate axis) and take the ground sideline center as the coordinate origin to establish the corresponding rectangular coordinate system. According to the principle of radio wave propagation and the research scope of the scenario, it is analyzed that the influence of rail, track, and inner fence on ray propagation can be ignored. Therefore, in order to reduce the calculation amount of RT, the scenario model is simplified and some curved models such as columns and elevators are simplified to plane models.

2.3. Ray-Tracing Simulation and Parameter Setting. RT is an electromagnetic environment prediction method based on geometric optics (GO) theory and uniform theory of diffraction (UTD). The basic principle is to simplify electromagnetic wave propagation as a ray model while considering optical mechanisms such as direct, reflection, scattering, diffraction, and transmission. By tracking each ray that reaches the receiving antenna within the scenario, it can describe the propagation path of radio waves through rays in optical theory under the condition that the scenario information is known, so as to obtain the multipath geometric parameters necessary for calculating electromagnetic characteristics, including ray power, delay, arrival angle, and departure angle. It has very broad application prospects both indoors and outdoors, such as stations, tunnels, and viaducts.

RT is one of the deterministic modeling methods, which depicts the dynamic changes in the channel state by setting snapshots at different positions. Therefore, the channel on each snapshot is static, and each snapshot can be used as a time slice. The following expressions about channel parameters will be expressed on the basis of snapshots.

The simulation sets have two trains (T1 and T2) on tracks 4 and 5, respectively, with T1 passing at a speed of 350 km/h and T2 remaining stationary. After the preliminary simulation analysis, it was found that the impact of diffraction on the wireless channel can be ignored, so the radio wave propagation mechanism only considers line-of-sight (LoS), reflection, and scattering. To balance the complexity and accuracy of the simulation, the reflection order is set to 2. This article assumes T1 as the transmitter and T2 as the receiver and sets 631 snapshots at 1 m intervals. T1 and T2 both use omnidirectional antennas with an antenna gain of 8 dB, which are installed in the center of the top of the headstock. The RT parameters are shown in Table 1.

The coordinate system of the simulation is calculated from the ground surface of the station, and 4.11 m not only includes the height of the train and the antenna but also includes the height of the railway track and the trackless bed, which is a total of 0.31 m, so the height of the antenna is 10 cm. The interval between snapshots is only 1 m, and it has been found that this does not improve the accuracy of the simulation results significantly and seriously affects the efficiency of the simulation by setting smaller intervals between snapshots during the simulation.

3. Analysis and Modeling of Wireless Channel Characteristics

Channel transfer function (CTF) and ray parameters can be obtained by RT simulation, where the ray parameters include electric field strength, time delays, and angles. Thus, the most preliminary ray-based channel impulse response (CIR) model can be obtained as shown in equation (1), where N represents the number of rays, τ_n, ω_n, and ψ_n, respectively, are the time delay, angle of arrival (AoA), and angle of departure (AoD) of the n_{th} ray, β_n is the complex amplitude of the n_{th} ray, and χ_n is the phase of the ray, which is a statistically independent random variable uniformly distributed over $[0, 2\pi)$.

$$h(t, \Theta_{\text{AoA}}, \Theta_{\text{AoD}}) = \sum_{n=1}^{N} \beta_n e^{j\chi_n} \delta(t - \tau_n) \tag{1}$$
$$* \delta(\Theta_{\text{AoA}} - \omega_n) * \delta(\Theta_{\text{AoD}} - \psi_n).$$

Then, the channel parameters can be extracted by data processing, including PDP, Rice factor K, and angular spread.

3.1. Propagation Path. Figure 3 shows the radio wave propagation path diagram at snapshots 100, 200, 300, 400, 500, and 600. At these locations, there are LOS paths, as well as reflection paths and scattering paths from the left and right platform pillars. When T1 approaches T2 (from snapshot 100 to snapshot 400), the number of rays gradually increases, and the number of rays is the highest when T1 and T2 are closest (i.e., at snapshot 400). As T1 moves away from T2 (from snapshot 400 to snapshot 600), the number of rays gradually decreases, and the ray propagation characteristics are roughly symmetric, centered around snapshot 400.

Table 1: RT parameter table.

Parameter	Value
Frequency band (GHz)	2.1
Bandwidth (MHz)	100
Resolution (MHz)	1
Propagation mechanisms	LoS, reflection, and scattering
Reflection order	2
Scattering mode	Directive mode
Type of train antenna	Horizontal omnidirectional antenna
Antenna gain (dB)	8
Antenna position of T1	$(2.5, 620 : -2 : 0, 4.11)$
Antenna position of T2	$(9, 401.75, 4.11)$
Train speed v (km/h)	350
Snapshot spacing d_s (m)	1

Since the antenna used is a horizontal omnidirectional antenna with a weak effect of signals reflected from the ceiling, the ray tracing only displays rays that are within the power threshold and rays with weaker power are not displayed. At a bandwidth of 100 MHz, the rays are difficult to distinguish in the time delay domain, but the high angular resolution of ray tracing allows the rays to be distinguished in the angular domain.

3.2. Path Loss.

Path loss refers to the loss of the received power relative to the transmitted power when the radio wave propagates. The path loss calculation formula based on RT simulation data is as follows:

$$PL(d) = \frac{N}{\sum_N |H_s(f)|^2}, \tag{2}$$

where $H_s(f)$ represents CTF at the s_{th} snapshot, N represents the number of the frequency points in the RT simulation, and d represents the distance from the transmitter at the s_{th} snapshot.

Theory and test data show that path loss usually increases logarithmically with distance. In addition, due to the difference of the surrounding environment in different locations, the shadow fading will occur randomly, and the free intercept path loss model is usually used as shown by the following equation:

$$PL(d) = A + 10n \lg(d) + X_\sigma, \tag{3}$$

where n is the path loss factor, indicating the rate at which the path loss increases with the distance; d is the transmit-receive distance; A is the intercept; and X_σ represents shadow fading.

Figure 4 shows the path loss data and its fitting graph. The logarithmic coordinate axis is used in the x-axis. It can be seen from the figure that the model has a good fitting effect.

Figure 5 shows the probability density function (PDF) distribution of the dB value of shadow fading. Currently, lognormal distribution is widely used to describe shadow fading. Its PDF is shown in the following equation:

$$f(x) = \frac{1}{\sqrt{2\pi}\sigma} \exp\left(-\frac{(x-\mu)^2}{2\sigma^2}\right), \tag{4}$$

where μ represents expectation and σ represents standard deviation.

The fitting parameters of the model are given in Table 2. The free intercept path loss model indicates that the intercept A and the path loss factor n change with the environment. The results show that the path loss factor ($n = 1.6$) in this scenario is smaller than that in the free space path loss factor ($n = 2$), indicating that the scenario of the high-speed railway station is relatively empty and semihermetic, the receiver-transmitter antennas are at the same height, and the LOS path propagation between vehicles is not obstructed. In addition to the LOS path, there are also high-power reflection and scattering paths, which increase the received power. Therefore, the path loss factor is less than n in free space. At the same time, A in this formula can be regarded as the combined effect of 32.4 and the mean value of shadow fading, and the mean value of shadow fading does not conclude μ which is fitted using the lognormal distribution. So the extra 5 dB can reflect that shadow fading still has a strong positive feedback effect on path loss.

3.3. PDP.

PDP represents the spectrum formed by the expected value of the received signal power at a certain time delay, reflecting the distribution of multipath power at different time delays. In this paper, the channel at each snapshot obtained by RT simulation can be considered static, and PDP is extracted based on CIR at each snapshot as follows:

$$\begin{aligned} P_s(\tau) &= |h_s(\tau)|^2, \\ h_s(\tau) &= \int_{-\infty}^{\infty} H_s(f) e^{j2\pi f \tau} \mathrm{d}f, \end{aligned} \tag{5}$$

where s represents the snapshot index, $P_s(\tau)$ presents PDP at the s_{th} snapshot, and $h_s(\tau)$ is CIR at the s_{th} snapshot.

The PDP at each snapshot is shown in Figure 6. We use the multipath component with the smallest delay τ as the normalization criterion. In this scenario, the LOS path always exits, so the power is strongest at 0 ns. The power here is in dB, which is for the channel. "dB" stands for a gain or loss. It represents the loss propagated solely by the channel path, not including the power of the transmitting antenna as well as the antenna gain. The PDP at different snapshot locations is significantly different, and the channel presents obvious nonstationary characteristics. The following rules can be found:

(1) At the low delay of less than 100 ns, the high-power multipaths appear at many snapshots, which are caused by the reflection and scattering effect of evenly and densely distributed pillars on both sides of the station.
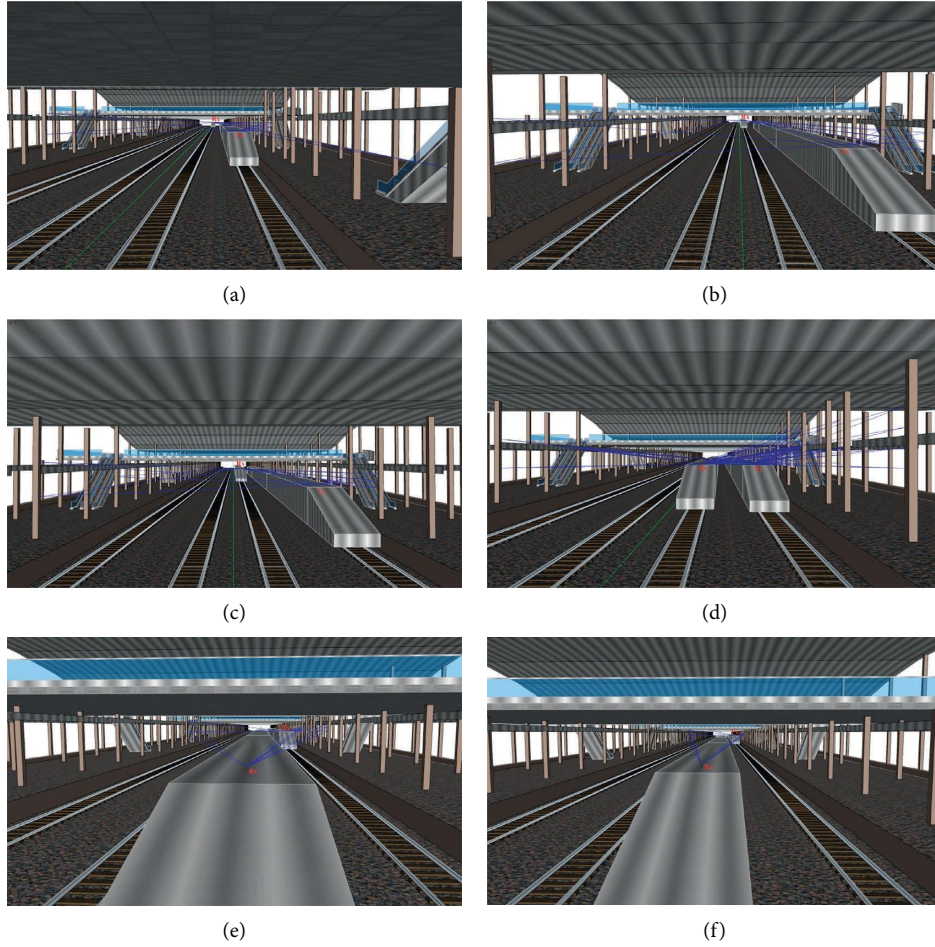
FIGURE 3: Propagation path at typical snapshots: the red markings represent the transmitter and receiver antenna positions, and the blue lines represent the ray propagation paths: (a) snapshot 100; (b) snapshot 200; (c) snapshot 300; (d) snapshot 400; (e) snapshot 500; (f) snapshot 600.

(2) As can be seen from the blue marked part of Figure 6, when the transmit-receive antenna distance is greater than 100 m, that is, snapshot 1 to snapshot 300, there are a lot of multipaths with relatively stable delay at 140 ns and 340 ns, and this is caused by the reflection and scattering of the left column (closest to track 2) and the right column (closest to track 5) of the station, respectively; there are multipaths at snapshot 500 to snapshot 631 with a delay of 370 ns, and it is caused by the reflection and scattering from the column on the right side of the platform.

(3) When the transmitter-receiver antenna distance is less than 100 m, that is, snapshot 300 to snapshot 500, the number of multipaths is large and the delay changes dramatically, which is caused by the simultaneous reflection and scattering of pillars on both sides of the platform.

3.4. Multipath Clustering and Tracking. In actual channels, multipath components (MPCs) often appear in clusters [18–20]. A cluster is defined as a set of MPCs with similar delay, arrival angle, and departure angle at the same time.

Cluster parameters usually remain unchanged for a period of time, which can reflect channel characteristics more accurately, especially suitable for nonstationary channel modeling. Therefore, the identification and modeling of clusters is an important aspect of current channel research.

From PDP shown in Figure 6, it can be seen that there are obvious nonstationary and MPCs clustering phenomena in the T2T channel in this paper. Based on the channel data obtained by RT, this paper adopts clustering and tracking algorithm to complete the modeling of clusters in time-varying nonstationary channels. The flowchart is shown in Figure 7.

(i) Firstly, the KPowerMeans algorithm is used to cluster the MPCs under each snapshot [21], and the centroids of the clusters under each snapshot and the MPC parameters within the clusters (power, delay, and azimuth angle and elevation angle of arrival and departure angles) are obtained.

(ii) Clusters of different snapshots have birth and death phenomena, including birth, death, and inheritance of clusters. The tracking algorithm [22, 23] based on the multipath component distance (MCD) is used to
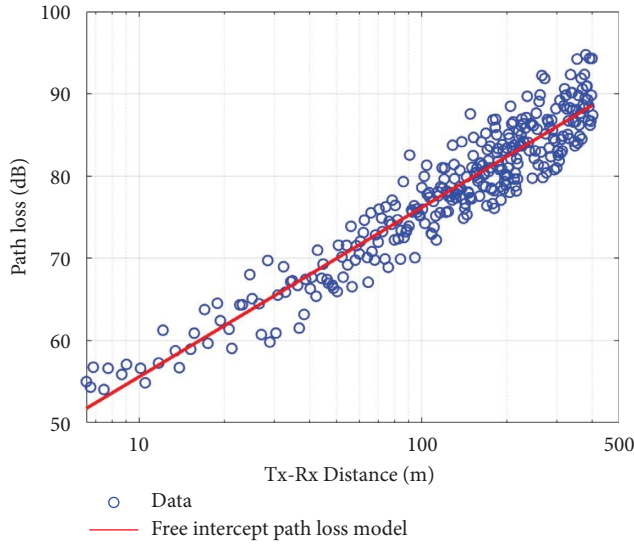
FIGURE 4: The blue dots represent the path loss obtained through RT simulation. The solid red line is the fitting result of the free intercept path loss model as shown in equation (3).
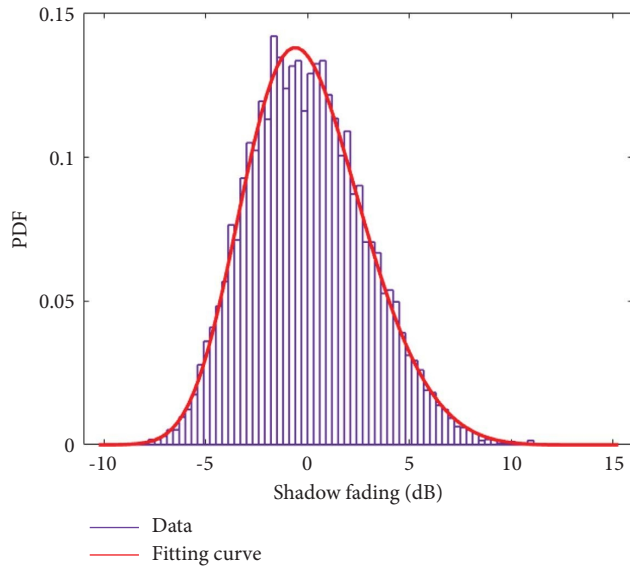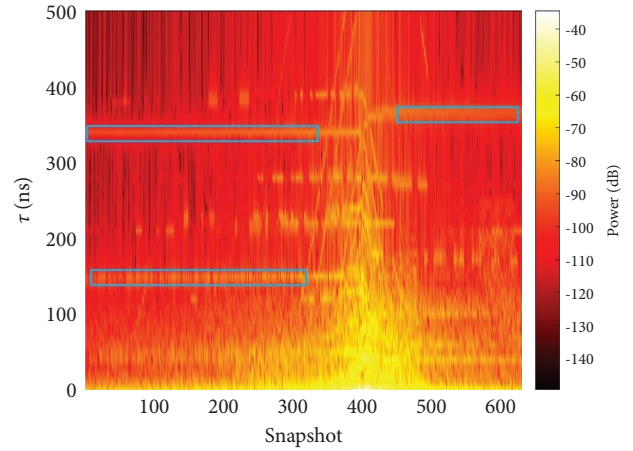

FIGURE 6: The PDPs of all snapshots: the x-axis represents the different snapshots, the y-axis represents the delay, and the colors represent the gain of the propagation paths.

FIGURE 5: The blue bars represent the shadow fading obtained through RT simulation. The solid red line is the fitting result of the shadow fading shown in equation (4).
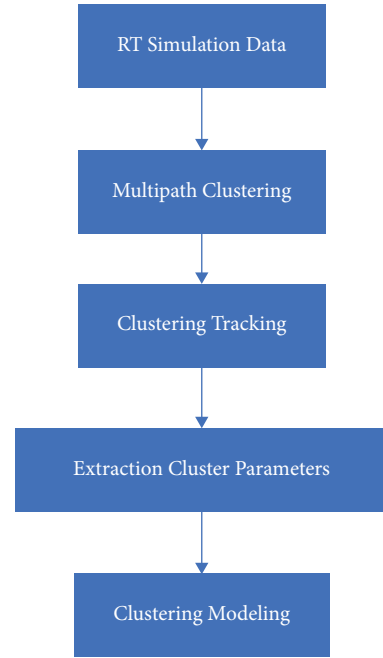

FIGURE 7: The flowchart of clustering and tracking: the above process represents the first step of the flowchart, and the second half of the subsection continues with steps 2–5.

(iii) Finally, according to the results of clustering and tracking, the intercluster and intracluster parameters of clusters are extracted to complete the modeling of clusters.

TABLE 2: Free intercept path loss model fitting parameters.

Parameter	Value
A (dB)	37.38
n	1.96
μ (dB)	−0.72
σ (dB)	2.89

judge the birth and death states of clusters at different snapshots, track the changes of clusters, and obtain time-varying clusters.

3.4.1. Multipath Clustering. The multipath clustering in this paper is mainly based on KPowerMeans algorithm. Firstly, the set of cluster centroids and cluster indexes of all MPCs in K clusters is obtained by the KPowerMeans algorithm. Then, the CombinedValidate algorithm is used to measure the

clustering effect by introducing two parameters, CH and DB indexes, and determine the optimal value of cluster number K_{opt}. Finally, a cluster pruning algorithm (ShapePrune) is used to discard the abnormal MPCs in the cluster.

Algorithm 1 shows the overall framework of multipath clustering, where K_{min} and K_{max} represent the minimum and maximum values of the cluster number, respectively, and R_K is the set of cluster centroids and cluster indexes of all MPCs of the specified cluster number as K, v_K is the clustering effect verification result of K clusters, R_{opt} is the set of cluster centroids and cluster indexes of all MPCs when the number of clusters is optimal, and R^p is the set of cluster centroids and cluster indexes of all MPCs after pruning clusters of R_{opt}.

3.4.2. KPowerMeans.

Based on the KMeans algorithm, the KPowerMeans algorithm considers the influence of power when calculating the distance of adjacent multipaths. The input parameters are the parameter matrix $X = [x_1, \ldots, x_L]$ of all L MPCs and the power matrix $P = [P_1, \ldots P_L]$, and the parameter vector x_l of each MPCs contains delay τ, AoA's azimuth angle and elevation angle $(\phi_{\text{AoA}}, \theta_{\text{AoA}})$, and AoD's azimuth angle and elevation angle $(\phi_{\text{AoD}}, \theta_{\text{AoD}})$.

For the specified K clusters, the algorithm randomly selects K initial cluster centroids $c_1^{(0)} \cdot c_K^{(0)}$, within the given maximum number of MaxIterations, first uses the MCD algorithm to find the closest cluster centroid to each MPC and store its corresponding cluster index in $I^{(i)}$, and then goes through the index of all MPCs' cluster centroids. The set $C^{(i)}$ of MPCs under each cluster centroid is obtained, and then the MCD algorithm is used to calculate the new cluster centroid $c_k^{(i)}$ of MPCs under each cluster centroid $c_k^{(i-1)}$ again, until all the calculated new cluster centroids are the same as the last iteration, and then the iteration process exits and the set R_K is returned; see Algorithm 2 for details.

The KPowerMeans algorithm uses MCD to calculate the distance between MPC (c_i) and cluster centroid (c_j). MCD calculates the angle and delay differently, as shown in equations (6) and (7), where θ_i represents the azimuth angle, φ_i represents the elevation angle, τ_i represents the delay, τ_{std} represents the standard deviation of the delay of all MPCs, and ζ is the delay scale factor, reflecting the importance of the time domain, in general, Equation $\zeta = 1$. Equation (8) gives the MCD distance considering the angle and delay.

$$\text{MCD}_{\text{AoA/AoD}}(c_i, c_j) = \frac{1}{2}\left|\begin{pmatrix} \sin(\theta_i)\cos(\varphi_i) \\ \sin(\theta_i)\sin(\varphi_i) \\ \cos(\theta_i) \end{pmatrix} - \begin{pmatrix} \sin(\theta_j)\cos(\varphi_j) \\ \sin(\theta_j)\sin(\varphi_j) \\ \cos(\theta_j) \end{pmatrix}\right|, \tag{6}$$

$$\text{MCD}_\tau(c_i, c_j) = \zeta \cdot \frac{|\tau_i - \tau_j|}{\Delta\tau_{\text{max}}} \cdot \frac{\tau_{\text{std}}}{\Delta\tau_{\text{max}}},$$
$$\Delta\tau_{\text{max}} = \max_{i,j}\left\{|\tau_i - \tau_j|\right\}, \tag{7}$$

$$\text{MCD}(c_i, c_j) = \sqrt{\left\|\text{MCD}_{\text{AoA,ij}}\right\|^2 + \left\|\text{MCD}_{\text{AoD,ij}}\right\|^2 + \text{MCD}_{\tau,\text{ij}}^2}. \tag{8}$$

3.4.3. CombinedValidate.

For the validation of clustering performance, CH and DB indexes are combined in this paper. The CH index is calculated as follows:

$$\text{CH}(K) = \frac{\text{tr}(B) \cdot (L - K)}{\text{tr}(W) \cdot (K - 1)}, \tag{9}$$

where $\text{tr}(\cdot)$ is the rank of the matrix, the matrices B and W represent the intercluster and intracluster scattering matrices, respectively, and the distance is calculated using the MCD algorithm. $\text{tr}(B)$ and $\text{tr}(W)$ can be calculated, respectively, as follows:

$$\text{tr}(B) = \sum_{k=1}^{K} L_k \cdot \text{MCD}^2(c_k, \bar{c}),$$
$$\text{tr}(W) = \sum_{k=1}^{K} \sum_{j \in C_k} \text{MCD}^2(x_j, c_k), \tag{10}$$

where L_k represents the number of MPCs in the k_{th} cluster and $\bar{c}$ represents the global cluster centroid of all MPCs:

$$\bar{c} = \frac{\sum_{l=1}^{L} P_l \cdot x_l}{\sum_{l=1}^{L} P_l}. \tag{11}$$

(1) **for** $K = K_{\min}, \ldots, K_{\max}$ **do**
(2)   Plan K clusters for the specified snapshot:
(3) $R_K = $ KPowerMeans (P, X, K)
(4)   Validate K clusters:
(5) $v_K = $ CombinedValidate (R_K)
(6) **end**
(7) Find optimum number of clusters:
(8) $K_{\mathrm{opt}} = \arg \max_{K v_K}$, $R_{\mathrm{opt}} = R_{K_{\mathrm{opt}}}$
(9) Prune optimum number cluster set:
(10) $R^p = $ ShapePrune (R_{opt})

ALGORITHM 1: Multipath clustering framework.

(1) Randomly choose K initial centroids $c_1^{(0)}, \ldots, c_K^{(0)}$
(2) **for** $i = 1, \ldots,$ MaxIterations **do**
(3)   Assign MPCs to cluster centroids and store indices:
(4)   **for** $l = 1, \ldots, L$ **do**
(5) $I_l^{(i)} = \arg \quad \min_k \{P_l \cdot \mathrm{MCD}(x_l, c_k^{(i-1)})\}$
(6)   **end**
(7) $I^{(i)} = [I_1^{(i)}, \ldots, I_L^{(i)}],$
(8)   **for** $k = 1, \ldots, K$ **do**
(9) $C_k^{(i)} = \mathrm{Indice}_l (I_l^{(i)} = k)$
(10)   **end**
(11) $C^{(i)} = [C_1^{(i)}, \ldots, C_K^{(i)}]$
(12)   Recalculate cluster centroids $c_k^{(i)}$ from the allocated MPCs to coincide with the clusters' centroids:
(13)   **for** $k = 1, \ldots, K$ **do**
(14) $c_k^{(i)} = (\sum_{j \in C_k^{(i)}} P_j \cdot x_j / \sum_{j \in C_k^{(i)}} P_j)$
(15)   **end**
(16)   **if** $c_k^{(i)} = c_k^{(i-1)}$ for all $k = 1, \ldots, K$ **then**
(17)   Return $R_K = [I^{(i)}, C^{(i)}]$
(18)   **end**
(19) **end**

ALGORITHM 2: KPowerMeans algorithm.

The DB index is calculated as follows:

$$\mathrm{DB}(K) = \frac{1}{K} \sum_{i=1}^{K} R_i, \tag{12}$$

where R_i is a function that describes the intracluster compactness S_k and the intercluster dispersion d_{ij}, as follows:

$$R_i = \max_{\substack{j=1,\ldots,K, \\ j \neq i}} \left\{ \frac{S_i + S_j}{d_{ij}} \right\},$$

$$S_k = \frac{1}{L_k} \sum_{l \in C_k} \mathrm{MCD}(x_l, c_k), \tag{13}$$

$$d_{ij} = \mathrm{MCD}(c_i, c_j).$$

In the combination of the two validation criteria introduced, this paper uses the minimum value in the DB index to restrict the set of optimal clusters to be selected. The CH index is then used to determine the optimal value of the cluster number in the set. Here, consider the set of the best number of clusters $F = K_1, \ldots, K_N \subseteq [K_{\min}, K_{\max}]$, and K_i needs to satisfy the following condition:

$$\mathrm{DB}(K_i) \leq 2 \cdot \min_K \{\mathrm{DB}(K)\}. \tag{14}$$

The optimal number of cluster K_{opt} is the value of K corresponding to the maximum CH index in the set:

$$K_{\mathrm{opt}} = \arg \max_{K \in F} \{\mathrm{CH}(K)\}. \tag{15}$$

3.4.4. ShapePrune. After the optimal cluster number is determined successfully, this paper uses the clustering pruning algorithm to remove the outliers. It is mainly achieved by deleting the data points with the largest distance from the cluster centroids, and the original power and shape of the clusters are restricted by the change of the power and the parameters of the clusters within a certain range, as shown in Algorithm 3.

First, the optimal cluster after clustering verification is initialized as the cluster to be pruned. For each cluster, the MPC power and the cluster power $P_k^{(0)}$ are recorded, and the

RMS delay and angular spread are recorded as the extension vector $S_k^{(0)}$. Here using s and k as the threshold factors respectively to be the weights of the initial cluster power $P_k^{(0)}$ and $S_k^{(0)}$. When the current cluster power $P_k^{(\text{cur})}$ and extension vector $S_k^{(\text{cur})}$ are greater than the given threshold power and extended threshold, based on MCD, the MPC farthest from the current cluster centroid is found and removed, and then the current cluster power and expansion vector are recalculated until the threshold limit is not met, and the set of cluster centroids and cluster indexes of all MPCs $R^{(p)}$ is returned.

3.4.5. Cluster Tracking.

The tracking algorithm of clusters is based on the distance between cluster centroids. Because the location of cluster centroids involves multidimensional parameter space (angle and delay), MCD is still chosen as the distance metric. Based on the clustering results obtained, cluster tracking is performed by checking the MCD between cluster centroids between adjacent locations, where M represents the number of snapshots. For each old cluster in the i_{th} snapshot, the nearest new cluster is found in the $(i + 1)_{\text{th}}$ snapshot. In turn, the nearest old cluster is determined for this new cluster. If the old and new clusters are both closest to each other and the MCD between them is below the predefined threshold η, then the two clusters are related. Otherwise, unrelated old clusters are considered "dead" and unrelated new clusters are considered "born." See Algorithm 4 for details.

3.4.6. Cluster Parameters Modeling.

According to the above processing method, the KPowerMeans algorithm can obtain the cluster centroids and MPCs information (power, delay, and azimuth angle and elevation angle of arrival angle and departure angle) under each snapshot, and the MCD-based tracking algorithm can obtain the inheritance relationship between clusters under different snapshots. Finally, the intercluster and intracluster parameters describing the distribution, density, and shape of clusters in the channel can be extracted. The intercluster parameters include the number, the arrival time, the life cycle, and the power delay attenuation factor of clusters. The intracluster parameters include the distribution and amount of intracluster MPCs, the delay spread of the cluster, and the angular spread. In this paper, the number, life cycle, arrival time of clusters and the amount of intracluster MPCs, and K factor for clusters are preliminarily modeled, and the results are as follows.

Clusters are divided into LOS clusters and reflection and scattering clusters. As shown in Figure 8, different snapshots have 1–6 clusters, respectively, with an average value of 2.3. Figure 6 only shows the display of multipath power in time delay domain. The multipath clustering used in this paper not only takes into account the factors of delay and power but also the effects of arrival and departure angles. Therefore, the clustering effect presented by PDP is only a partial display of the clustering algorithm in time delay domain.

The life cycle of a cluster is defined as the time that a cluster experiences from birth snapshot a to death snapshot b, as follows:

$$\text{cluster life} = \frac{(b - a) \cdot d_s}{v}. \tag{16}$$

The CDF of the life cycle of the reflection and scattering clusters is given in Figure 9, with an average value of 21.6 ms, which is about 1.05 snapshots. The longest duration is 6 snapshots. The shorter the duration of the cluster is, the worse the channel stationarity is. The channel will undergo drastic changes in a short period of time, and the MPCs in the cluster also change rapidly. This is also consistent with many evenly spaced arrayed reflectors and scatters in the scenario. These reflectors and scatters have a great impact on the T2T channel and greatly reduce the survival time of the cluster. The birth and death of the cluster are closely related to the stationarity of the channel, which also affects the time interval of the receiver's estimation of the channel indirectly.

Based on the life cycle of clusters, the distribution of clusters can be accurately obtained by modeling the arrival time of clusters. The arrival time of the cluster is defined as the moment when the cluster is born, that is, the time from the start of the train to the birth of the cluster. The CDF of the arrival time of all clusters is given in Figure 10. It can be seen that the time interval of cluster arrival time can be approximately uniformly distributed, which means that the clusters will appear evenly during the entire process, with an average of 1.09 new clusters per snapshot birthing. By converting snapshot spacing and speed into time, an average of 54.5 clusters per second are born.

The amount of intracluster MPCs represents the number of multipaths contained inside each cluster, and the CDF of the number of MPCs per cluster is given in Figure 11. 50% of the amount of intracluster MPCs are within 8 paths, and the remaining can be as high as 60. The mean value of the amount of intracluster MPCs in the station scenarios is 14.35, and the standard deviation is 15.71.

The K factor of the cluster is used to describe the power ratio of the dominant component to other components in the cluster, as shown in equation (17), where M represents the total number of MPCs in the cluster, a_0 represents the amplitude of the dominant path, and a_m represents the sum of the amplitude of the other MPCs in the cluster. The CDF of the K factor of the cluster is given in Figure 12, which shows that the K factor of the cluster obeys the normal distribution, and the mean of the K factor of the cluster in the station scenario is -5.52 dB and the standard deviation is 3.37 dB.

$$K = 10 * \log_{10}\left(\frac{|a_0|^2}{\sum_{m=1}^{M-1}|a_m|^2}\right). \tag{17}$$

Based on the above analysis, therefore a time-varying dynamic cluster-based channel model is proposed on the results after clustering and tracking as follows:

(1) Initialize the pruning set as an optimal clustering:
(2) $R^{(p)} = R_{\text{opt}}$
(3) **for** $k = 1, \ldots, K_{\text{opt}}$ **do**
(4)   Retain the initial power and parameters of the k th cluster:
(5) $P_k^{(0)} = \sum_{j \in C_k} P_j$,
                $S_k^{(0)} = [\sigma_\tau, \sigma_{\phi_{\text{AoA}}}, \sigma_{\phi_{\text{AoD}}}, \sigma_{\theta_{\text{AoA}}}, \sigma_{\theta_{\text{AoD}}}]^T$,
(6)   **while** $P_k^{(\text{cur})} > p \cdot P_k^{(0)} \; And \; S_k^{(\text{cur})} > s \cdot S_k^{(0)}$ **do**
(7)   Find MPC with largest distance to current centroids c_k;
(8)   Remove MPC from $R^{(p)}$;
(9)   Recalculate $P_k^{(\text{cur})}$ and $S_k^{(\text{cur})}$
(10)   **end**
(11)   Restore the last deleted MPC
(12) **end**
(13) Return $R^{(p)}$

ALGORITHM 3: ShapePrune algorithm.

(1) **for** $i = 1, \ldots, M - 1$ **do**
(2)   Gets the cluster centroids of the current snapshot $c_k^{(i)}$ and the next snapshot $c_k^{(i+1)}$:
(3)   **for** $a \in c_k^{(i)}$ **do**
(4)   Find the cluster closest to the next snapshot:
(5) $b_n = \arg\min_{c \in c_k^{(i+1)}} (\text{MCD}(a, c_k^{(i+1)}))$,
(6)   Returns to find the cluster closest to the snapshot:
(7) $a_n = \arg\min_{c \in c_k^{(i)}} (\text{MCD}(b_n, c_k^{(i)}))$
(8)   **if** $a_n = a$ and $\text{MCD}(a, b_n) \leq \eta$ **then**
(9) a and b_n can be regarded as a cluster
(10)   **end**
(11)   **end**
(12)   Update the set of clusters
(13) **end**

ALGORITHM 4: Tracking algorithm.
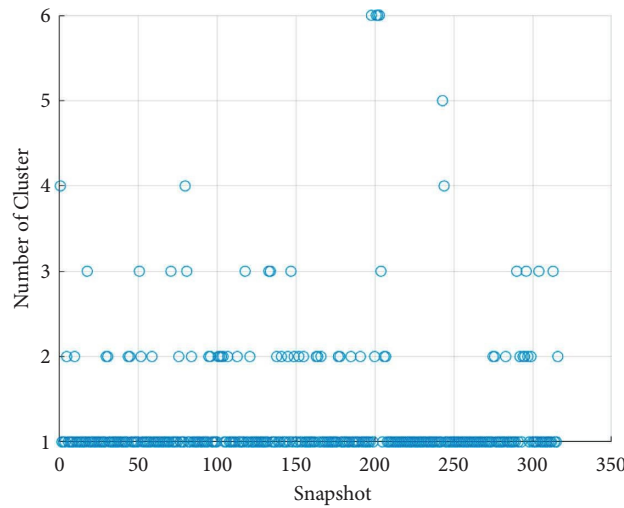
FIGURE 8: The x-axis represents the different snapshots and the y-axis represents the number of clusters for each snapshot.
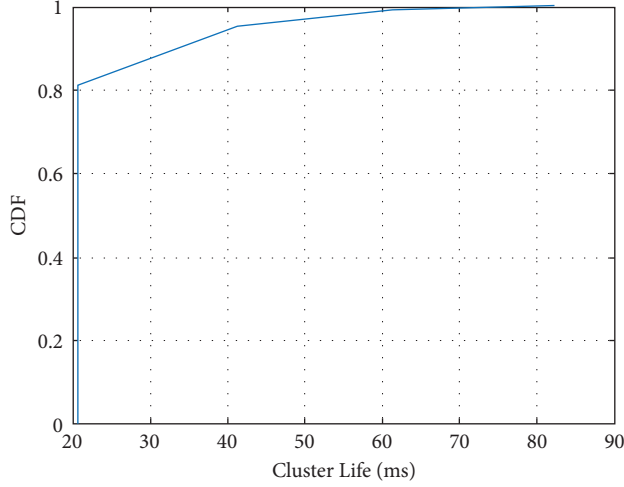
FIGURE 9: The solid blue line is the CDF of the cluster life.
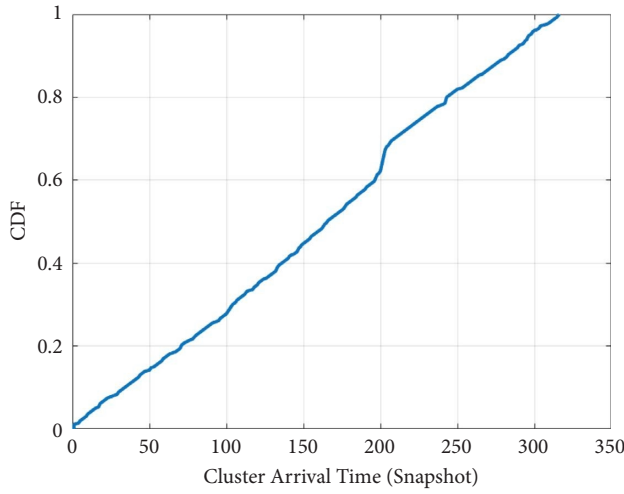

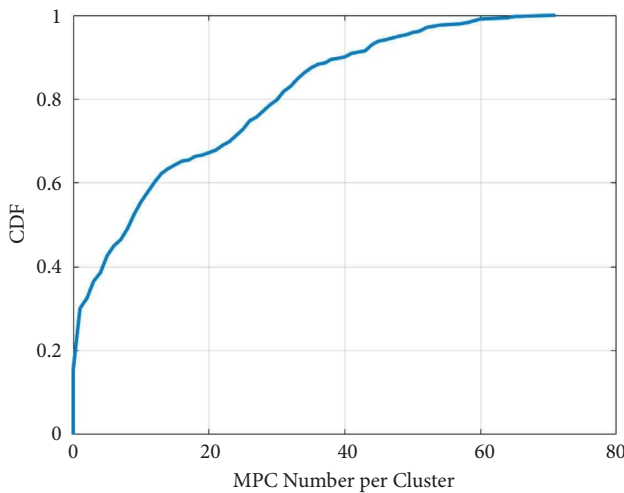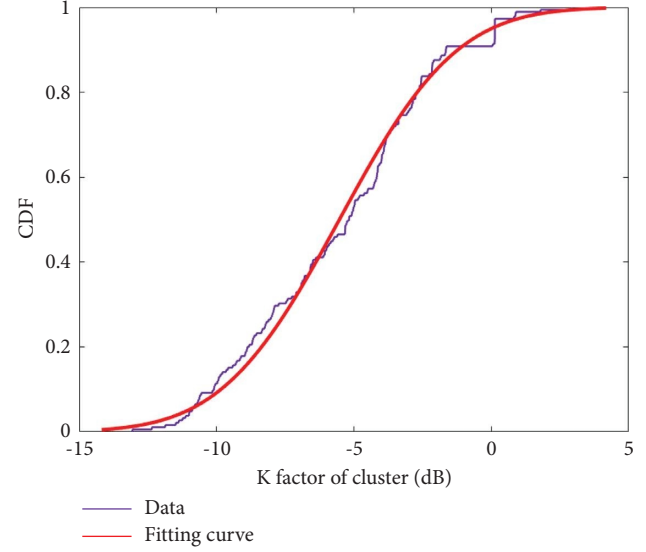FIGURE 10: The solid blue line is the CDF of the cluster arrival time.

FIGURE 11: The solid blue line is the CDF of the amount of intracluster MPCs.

FIGURE 12: The blue dots represent the K factor of the cluster obtained through RT simulation. The solid red line is the fitting result of the K factor of the cluster by using normal distribution.

$$
\begin{aligned}
h(t, &\Theta_{\mathrm{AoA}}, \Theta_{\mathrm{AoD}}) \\
&= \sum_{l=1}^{L} \sum_{k=1}^{K_l} \beta_{k,l} e^{j\chi_{k,l}} \delta(t - \tau_l - \tau_{k,l}) \\
&\quad \times \delta(\Theta_{\mathrm{AoA}} - \Omega_l - \omega_{k,l}) \delta(\Theta_{\mathrm{AoD}} - \Psi_l - \psi_{k,l}),
\end{aligned}
\tag{18}
$$

where L represents the number of clusters, K_L represents the number of rays of the L_{th} cluster, τ_l, Ω_l, and Ψ_l are, respectively, the time delay, AoA, and AoD of the L_{th} cluster, $\tau_{k,l}$, $\omega_{k,l}$, and $\psi_{k,l}$, respectively, are the time delay, AoA, and AoD of the l_{th} cluster, $\beta_{k,l}$ is the complex amplitude of the k_{th} ray in the l_{th} cluster, and $\chi_{k,l}$ is the phase of the ray, which is a statistically independent random variable uniformly distributed over $[0, 2\pi)$. Future work will further analyze the power and time-space characteristics of clusters.

3.5. Delay Spread.

In the wireless channel, the ray from the transmitting antenna to the receiving antenna propagating on different paths will lead to different delays. Large delay extension will lead to severe intersymbol interference (ISI), which will cause the performance of the communication system to be seriously degraded. Based on RT simulation data, the RMS delay spread in this scenario is explored. Using the delay τ of different rays and the power under this delay, the average and RMS delay spread can be obtained as follows:

$$
\begin{aligned}
T_m(s) &= \frac{\sum_{i=1}^{n(s)} P_s(\tau_i) \tau_i}{\sum_{i=1}^{n(s)} P_s(\tau_i)}, \\
S_\tau(s) &= \sqrt{\frac{\sum_{i=1}^{n(s)} P_s(\tau_i) \tau_i^2}{\sum_{i=1}^{n(s)} P_s(\tau_i)} - T_m(s)^2},
\end{aligned}
\tag{19}
$$

where $n(s)$ is the number of rays at the s_{th} snapshot and $P_s(\tau_i)$ represents the power of the i_{th} ray at the s_{th} snapshot under the delay. $T_m(s)$ and $S_\tau(s)$ represent the average delay and RMS delay spread at the s_{th} snapshot, respectively. Figure 13 shows the change of RMS delay spread with the distance between receiver-transmitter antennas and its fitting curve. The following rules can be found.

Overall, the RMS delay spread is large, with a value of 39.56 ns, which is closely related to the rich MPCs in the station scenario. Near snapshot 400, the RMS delay spread is the smallest, when the path loss of the LOS path between the receiver-transmitter antennas is the smallest, and the LOS path power is much larger than the reflection and scattering power. In other snapshots, the reflection and scattering have relatively larger power and larger delay spread.

There is a close relationship between RMS delay spread and transmitting-receiving distance. The literature [24] deduces and finds out that the RMS delay spread is proportional to the receiver-transmitter distance by measuring the data of the multipath delay spread in the LOS case in an urban environment, and at the same time, explains why this happens. This is a very new research direction, which shows that wireless channel characteristics are not only path loss affected by distance but multipath delay spread, Rice factor, and angle spread are also correlated with the receiver-transmitter distance, but the relationship between them in different scenarios cannot be fitted by a uniform expression, which is different from path loss. Here, a polynomial function is used for fitting, as shown in the following equation:

$$S_\tau = p_1 d^3 + p_2 d^2 + p_3 d + p_4 + X_1, \tag{20}$$

where S_τ is the RMS delay spread, p_1, p_2, p_3, and p_4 are the fitting coefficients, and X_1 is the residual of the RMS delay spread fitting. The fitting coefficients are shown in Table 3.

Other fitting effects have been tried, the fitting is still relatively more consistent with the change of RMS delay spread, the RMS delay spread presented here has a relationship with the receiver-transmitter distance, but this relationship is not fully deterministic, and there is no uniform fixed expression. The larger fluctuation of RMS delay spread under the same receiver-transmitter distance also shows that the receiver-transmitter distance is only a part of the factors affecting its variation, and the RMS delay spread is also related to the distribution of the surrounding reflectors, and the station scenario is dense in scatterers, with abundant multipaths, and there is a large amount of randomness in the RMS delay spread, which leads to a larger RMSE.

3.6. Rice Factor.
The Rice factor K reflects the power ratio of the dominant (or LOS) component to the other (or NLOS) component in a snapshot. The LOS and NLOS components always exist in this scenario, and $|a_0|^2$ in equation (17) can be replaced with P_{LoS} more accurately. Therefore, K can be expressed as follows [25]:
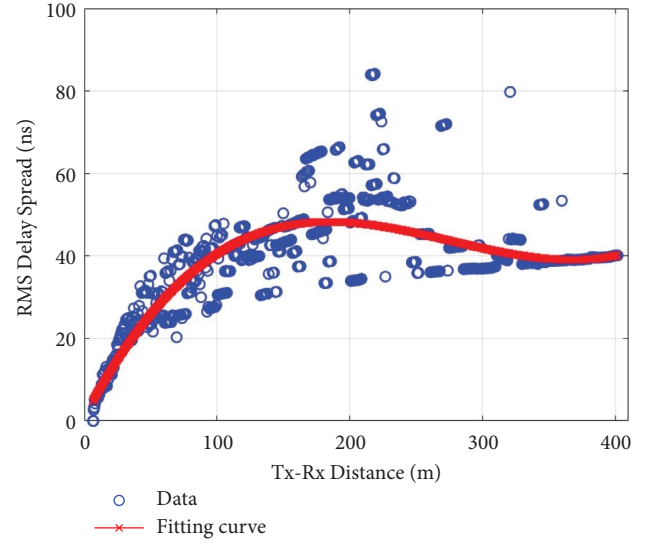

FIGURE 13: The blue dots represent the RMS delay spread obtained through RT simulation. The solid red line is the fitting result of the RMS delay spread as shown in equation (20).

TABLE 3: RMS delay spread fitting coefficient and accuracy.

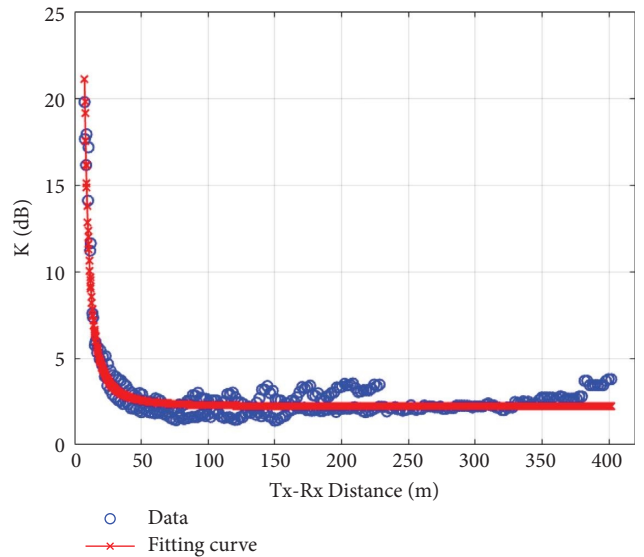| Fitting coefficient and accuracy	Value
p_1	3.91
p_2	−11.40
p_3	2.84
p_4	48.07
RMSE	8.03

FIGURE 14: The blue dots represent the Rice factor K obtained through RT simulation. The solid red line is the fitting result of the Rice factor K as shown in equation (22).

TABLE 4: K fitting coefficient and accuracy.

Fitting coefficient and accuracy	Value
a	708.90
b	−1.96
c	2.27
RMSE	0.7

$$K\,(\mathrm{d}B) = 10\lg\frac{P_{\mathrm{LoS}}}{P_{\mathrm{NLoS}}}, \tag{21}$$

where P_{LoS} represents the LOS component power and P_{NLoS} represents the reflection and scattering component power. Figure 14 shows the variation of K along with the distance between receiver-transmitter antennas and their fitting curves. The following rules can be found.

When the distance between receiver-transmitter antennas is less than 100 m, the K changes significantly with the distance. When the receiver-transmitter antenna distance exceeds 100 m, the K remains basically unchanged at around 2.27 dB. The negative exponential distribution is used to fit the change of K with the receiver-transmitter antennas distance, and the expression is shown as follows:

$$K = a * d^b + c + X_2, \tag{22}$$

where a, b, and c are the fitting coefficients and X_2 is the fitting residual of K, whose fitting coefficients are shown in Table 4.

3.7. Space Characteristics: RMS Angular Spread. The signals leave the transmitting antenna through different paths to the receiving antenna, and the angles of the reflected and scattered signals are different on different paths, which will form the angular spread of the arrival angle and the departure angle. Angular spread describes the energy and spatial distribution characteristics of the signal as it leaves and arrives at the antenna. Taking AoA as an example, the mean value and angular spread of the azimuth angle ϕ and the elevation angle θ of the arrival and departure angles, as shown in the following equation:

$$\mu_\phi(s) = \frac{\sum_{i=1}^{n(s)}\mathrm{APS}(s, \phi_i)\phi_i}{\sum_{i=1}^{n(s)}\mathrm{APS}(s, \phi_i)},$$

$$S_\phi(s) = \sqrt{\frac{\sum_{i=1}^{n(s)}\mathrm{APS}(s, \phi_i)\phi_i^2}{\sum_{i=1}^{n(s)}\mathrm{APS}(s, \phi_i)} - \mu_\phi(s)^2},$$

$$\mu_\theta(s) = \frac{\sum_{i=1}^{n(s)}\mathrm{APS}(s, \theta_i)\theta_i}{\sum_{i=1}^{n(s)}\mathrm{APS}(s, \theta_i)}, \tag{23}$$

$$S_\theta(s) = \sqrt{\frac{\sum_{i=1}^{n(s)}\mathrm{APS}(s, \theta_i)\theta_i^2}{\sum_{i=1}^{n(s)}\mathrm{APS}(s, \theta_i)} - \mu_\theta(s)^2},$$

where $n(s)$ is the number of rays at the s_{th} snapshot, APS represents the angle power spectrum, $\mu_\varphi(s)$ and $\mu_\theta(s)$ represent the average azimuth and average elevation angle at the s_{th} snapshot, respectively, and $S_\varphi(s)$ and $S_\theta(s)$ represent the RMS angular spread of the azimuth and elevation angles at the s_{th} snapshot, respectively.

Figure 15 shows the RMS angular spread of each snapshot, in which ASA, ESA, ASD, and ESD, respectively, represent the RMS angular spread of the azimuth and elevation angle of arrival, azimuth, and elevation angle of departure. Table 5 gives the median values of ASA, ESA, ASD, and ESD.

(1) As shown in Figure 15, the RMS angular spread of the azimuth is bigger, especially the azimuth angle of the departure. The ray is emitted from T1 to all sides through the reflection and scattering of the left and right columns, and it finally reaches T2 in a certain angle range.

(2) Regardless of the arrival angle or departure angle, the RMS angular spread of the elevation angle is very small, and the elevation angle of MPCs vary around 90°, almost parallel to the ground.

(3) ASA and ESA change irregularly and have no relationship with receiver-transmitter antenna distance, while ASD and ESD, such as the K factor, only change with the receiver-transmitter antenna distance when the distance is less than 100 m.

(4) Here, the relationship between ASD, ESD, and the receiver-transmitter antenna distance is fitted by a power approximation curve, as shown in equation (24), where X_3 is the fitting residual, a, b, and c are the fitting coefficients, and C is the constant. The fitting results are shown in Figure 16. The fitting coefficients are shown in Table 6. According to the fitted curve and formula, ASD, ESD, and d are positively correlated.

$$\mathrm{Angle\_spread} = a * d^b + c + X_3. \tag{24}$$

3.8. Nonstationarity. There is often a relative motion between the receiver-transmitter and the reflector-scatterer antennas, especially in the highly dynamic environment, and the channel will show nonstationarity, mainly in the statistical characteristics of the channel will change with time. The existing channel model based on WSSUS hypothesis cannot accurately describe the statistical characteristics of the channel, so it is very important to use a reasonable method to accurately describe the nonstationary wireless channel.

Channel quasi-stationary interval is an important parameter of the nonstationary characteristics of wireless channels, and the characteristics of wireless channels do not change greatly within the interval. Currently, many research studies on channel quasi-stationary interval are based on the analysis methods of the local scattering function (LSF) and
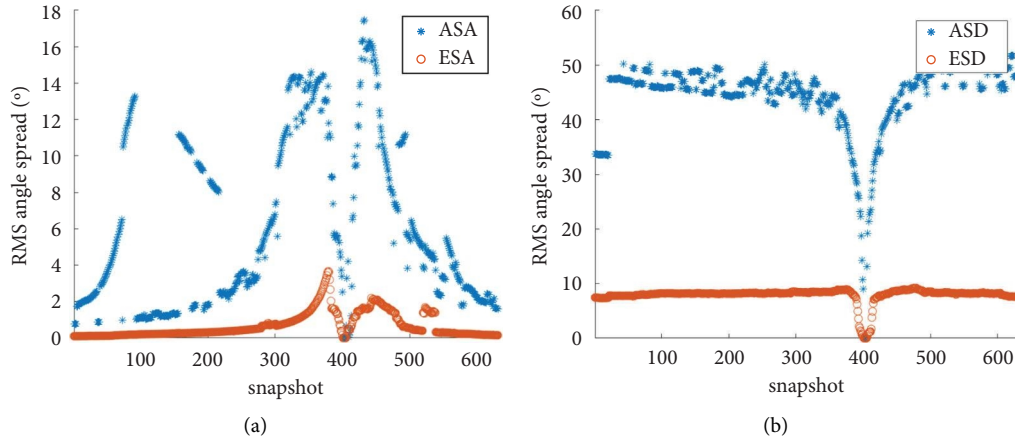
FIGURE 15: RMS angular spread: ASA, ESA, ASD, and ESD, respectively, represent the RMS angular spread of the azimuth and elevation angle of arrival and azimuth and elevation angle of departure. (a) ASA and ESA of AoA for all snapshots. (b) ASD and ESA of AoD for all snapshots.

TABLE 5: Median of RMS angular spread.

Parameter	Value
ASA	4.62°
ESA	0.34°
ASD	46.16°
ESD	8.19°

TABLE 6: ASD and ESD fitting coefficients and accuracy.

Fitting coefficient and accuracy	ASD	ESD
a	−467.20	−465.30
b	−1.24	−2.04
c	47.39	8.26
RMSE	3.46	0.51

time-varying coherence function [26]. The basic idea is to use the second-order statistical characteristics of the channel to find the correlation and difference degree of the channel.

For MIMO channels, correlated matrix distance (CMD) is a common method to calculate the quasi-stationary interval [27]. By calculating the correlation matrix of the receiver or the transmitter, the quasi-stationary interval is obtained by using the decision threshold. For SISO channels, the correlation of power (CP) algorithm can be used to calculate the correlation at different sampling points [28], and the quasi-stationary interval can be obtained by setting the threshold decision.

Since the simulation is investigating a single transmitter and single receiver station channel, the PDP at each snapshot can be used to calculate the correlation of the channel at different snapshots by using delay and power. In this paper, he CP algorithm is adopted, and TPCC is used as the measure of channel stationarity. According to the definition of [29], the TPCC of PDP in the s_i and s_j snapshots is as follows:

$$c\left(s_i, s_j\right) = \frac{\left[\sum_\tau P\left(s_i, \tau\right)\right] * \left[\sum_\tau P\left(s_j, \tau\right)\right]}{\max\left\{\sum_\tau P\left(s_i, \tau\right)^2, \sum_\tau P\left(s_j, \tau\right)^2\right\}}. \quad (25)$$

Among them, $P\left(s_i, \tau\right)$ is the power in s_i snapshot and τ delay. Obviously, the value of TPCC is in the range of 0 to 1. The closer the TPCC value is to 1, the higher the channel similarity between the s_i and s_j snapshots, and the higher the channel stationarity is. The relationship between snapshot and time is used to transform, and finally, Figure 17 is given to depict the TPCC of each moment and other moments.

When the receiver-transmitter antenna distance is less than 100 m (corresponding to t 3.1 s–5 s), the correlation of the channel is low, the existence of MPCs in the channel is single and stable, and the quasi-stationary distance of the channel is small. When the receiver-transmitter antenna distance is greater than 100 m (corresponding to t after 0 s–3 s and 5.1 s), the channel correlation is high, the channel MPCs delays change sharply, and the channel quasi-stationary distance is large, as shown in the red area of Figure 17.

According to the threshold selection policy [30], in this scenario, the threshold is set to 0.8 to extract the quasi-stationary distance of the channel. The quasi-stationary distance of the channel at each snapshot is given in Figure 18. The average quasi-stationary distance of the channel is 4.9 m, and the corresponding quasi-stationary time can be obtained as 50 ms by using the time-distance conversion formula. This is close to the measured results of the study in [31] on the average quasi-stationary distance of vehicle-vehicle communication channels and quasi-stationary time for T2T communication in the study in [15]. The quasi-stationary time between vehicles and vehicles in the highway is 23 ms. The results are in the same order of magnitude, but the number of scatterers between vehicles and vehicles in the highway is higher than that between trains in the high-speed railway, and the varieties of
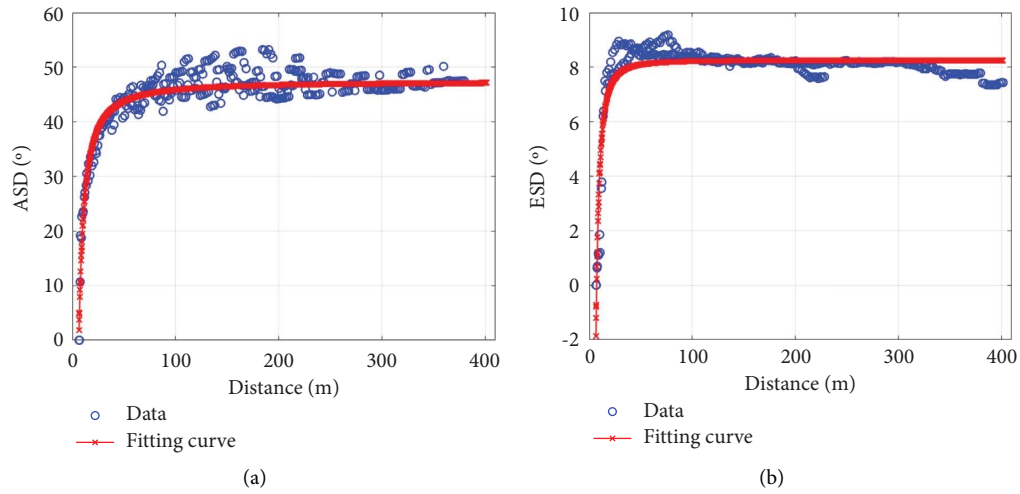
FIGURE 16: ASD and ESD. (a) The blue dots represent ASD obtained through RT simulation. (b) The blue dots represent ESD obtained through RT simulation. The solid red line is the fitting result of ASD and ESD as shown in equation (24).
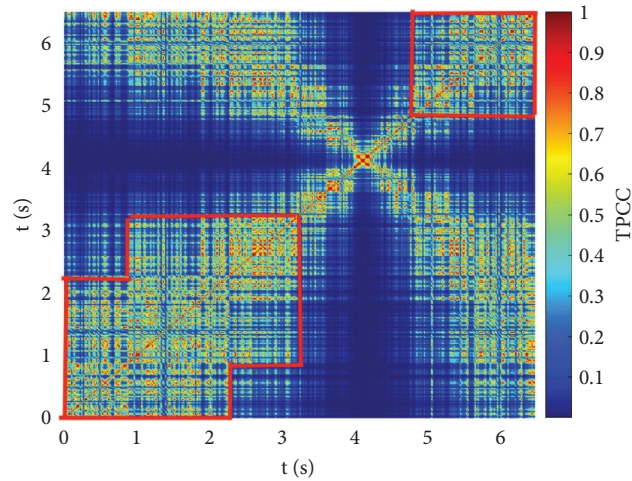

FIGURE 17: TPCC between every two moments: both the *x*-axis and *y*-axis represent time, and the color represents the size of the TPCC.
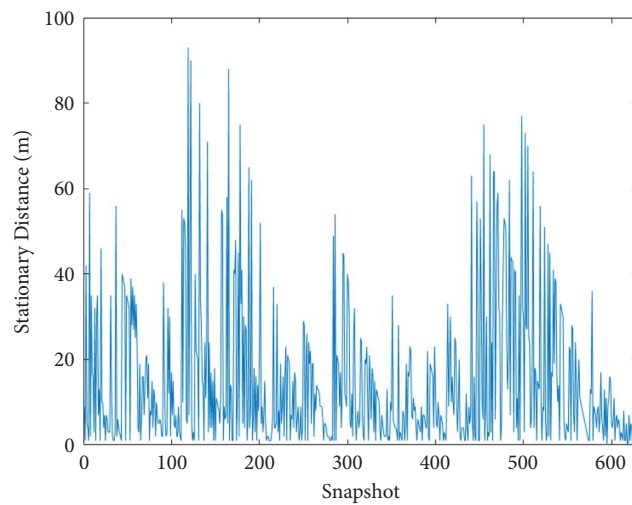

FIGURE 18: The *x*-axis represents the different snapshots and the *y*-axis represents the stationary distance for each snapshot.

TABLE 7: Channel modeling parameters.

Parameter	n	Shadow fading mean value (dB)	Shadow fading standard deviation (dB)	RMS delay spread median (ns)	K median (dB)	ASA median (°)	ESA median (°)	ASD median (°)	ESD median (°)
Value	1.96	−1.11	2.82	39.56	2.33	4.62	0.34	46.16	8.19

scatterers are rich. For example, there will be other vehicles as well as isolation zones between the vehicles and vehicles, the LOS path is not continuous, and the change of the NLOS path will be quicker and more pronounced, which will result in the quasi-stationary time to be smaller. In the study in [15], through field measurements, it was found that the stationary time of communication between the trains at the station is 65.5 ms. Considering the differences in the two communication environments, the quasi-stationary time of the 50 ms channel obtained in this study is also close to it.

After the analysis of channel nonstationarity, it can be drawn with the previous viaduct scenario [32]. For a more detailed conclusion, the influence of the signal transmission environment on channel stationarity is external, and the birth and death of MPCs have a more direct impact on channel stationarity. The unstable change of MPCs in a short time is an important reason that leads to the decrease of the stationarity of the channel.

4. Conclusion

Based on the RT technology, this paper studies the characteristics of wireless channels between high-speed trains in the 2.1 GHz band at the station scenario and establishes a channel model to provide theoretical support for T2T channel research. Future work will continue to study and analyze the characteristics of the channel between two trains moving at the same time and analyze the performance of communication systems such as channel capacity. The summary parameters of the channel model are shown in Table 7. The following conclusions are drawn:

(i) The path loss is log-linear with the distance between the receiver-transmitter antennas. The path loss factor is 1.96, and the shadow fading is more inclined to the generalized extreme value distribution.

(ii) Multipath clustering is realized, and the number and life cycle of clusters are preliminarily quantified. Within a certain receiver-transmitter antenna distance, the RMS delay spread is a polynomial distribution, and the Rice factor and angular spread of departure are power exponential distribution.

(iii) When the distance between trains is relatively close, the channel correlation is low, the channel changes rapidly and violently, and the number of MPCs is large. When the distance between trains is higher, the channel correlation is bigger.

(iv) The receiver needs to perform at least one estimation within a given quasi-stationary time interval (50 ms); otherwise, the channel estimation results will have obvious errors. This is the reason that leads

to the deterioration of communication performance in high-speed railway scenarios, which needs to be considered in the system design.

Data Availability

The data that support the findings of this study are available from the corresponding author upon reasonable request.

Conflicts of Interest

The authors declare that there are no conflicts of interest regarding the publication of this paper.

Acknowledgments

References

[1] A. Hrovat, G. Kandus, and T. Javornik, "A survey of radio propagation modeling for tunnels," *IEEE Communications Surveys & Tutorials*, vol. 16, no. 2, pp. 658–669, 2014.

[2] Y. Liu, A. Ghazal, C. Wang, X. Ge, Y. Yang, and Y. Zhang, "Channel measurements and models for high-speed train wireless communication systems in tunnel scenarios: a survey," *Science China Information Sciences*, vol. 60, no. 10, pp. 101301–101317, 2017.

[3] K. Guan, B. Ai, B. Peng et al., "Towards realistic high-speed train channels at 5G millimeter-wave band-part I: paradigm, significance analysis, and scenario reconstruction," *IEEE Transactions on Vehicular Technology*, vol. 67, no. 10, pp. 9112–9128, 2018.

[4] C.-X. Wang, J. Bian, J. Sun, W. Zhang, and M. Zhang, "A survey of 5G channel measurements and models," *IEEE Communications Surveys & Tutorials*, vol. 20, no. 4, pp. 3142–3168, 2018.

[5] T. Zhou, C. Tao, S. Salous, and L. Liu, "Measurements and analysis of angular characteristics and spatial correlation for high-speed railway channels," *IEEE Transactions on Intelligent Transportation Systems*, vol. 19, no. 2, pp. 357–367, 2018.

[6] X. Yin, X. Cai, X. Cheng, J. Chen, and M. Tian, "Empirical geometry-based random-cluster model for high-speed-train

channels in UMTS networks," *IEEE Transactions on Intelligent Transportation Systems*, vol. 16, no. 5, pp. 2850–2861, 2015.

[7] D. He, B. Ai, K. Guan et al., "Influence of typical railway objects in a mmWave propagation channel," *IEEE Transactions on Vehicular Technology*, vol. 67, no. 4, pp. 2880–2892, 2018.

[8] J. Yang, B. Ai, K. Guan et al., "A geometry-based stochastic channel model for the millimeter-wave band in a 3GPP high-speed train scenario," *IEEE Transactions on Vehicular Technology*, vol. 67, no. 5, pp. 3853–3865, 2018.

[9] K. Guan, Z. Zhong, B. Ai, and T. Kürner, "Propagation measurements and modeling of crossing bridges on high-speed railway at 930 MHz," *IEEE Transactions on Vehicular Technology*, vol. 63, no. 2, pp. 502–517, 2014.

[10] A. Saleem and Y. He, "Investigation of massive MIMO channel spatial characteristics for indoor subway tunnel environment," in *Proceedings of the 2021 Computing, Communications and IoT Applications (ComComAp)*, pp. 162–167, Shenzhen, China, November 2021.

[11] A. Saleem, Y. Xu, R. A. Khan, I. Rasheed, Z. U. A. Jaffri, and M. A. Layek, "Statistical characteristics of 3D MIMO channel model for vehicle-to-vehicle communications," *Wireless Communications and Mobile Computing*, vol. 2022, Article ID 9090494, 14 pages, 2022.

[12] P. Unterhuber, M. Walter, and T. Kürner, "Geometry-based stochastic channel model for train-to-train communication in open field environment," in *Proceedings of the 2022 16th European Conference on Antennas and Propagation (EuCAP)*, pp. 1–5, Madrid, Spain, March 2022.

[13] M. Soliman, P. Unterhuber, S. Sand et al., "Dynamic train-to-train propagation measurements in the millimeter wave band-campaign and first results," in *Proceedings of the 2019 13th European Conference on Antennas and Propagation (EuCAP)*, pp. 1–5, Krakow, Poland, March 2019.

[14] E. M. Bigñotte, P. Unterhuber, A. A. Gómez, S. Sand, and M. M. Errasti, "Measurement based tapped delay line model for train-to-train communications," *IEEE Transactions on Vehicular Technology*, vol. 72, no. 4, pp. 4168–4181, 2023.

[15] P. Unterhuber, M. Walter, U.-C. Fiebig, and T. Kürner, "Stochastic Channel parameters for train-to-train communications," *IEEE Open Journal of Antennas and Propagation*, vol. 2, pp. 778–792, 2021.

[16] C. Briso-Rodríguez, P. Fratilescu, and Y. Xu, "Path loss modeling for train-to-train communications in subway tunnels at 900/2400 MHz," *IEEE Antennas and Wireless Propagation Letters*, vol. 18, no. 6, pp. 1164–1168, 2019.

[17] K. Guan, B. Peng, D. He et al., "Channel sounding and ray tracing for train-to-train communications at the THz band," in *Proceedings of the 2019 13th European Conference on Antennas and Propagation (EuCAP)*, pp. 1–5, Krakow, Poland, March 2019.

[18] T. Zwick, C. Fischer, D. Didascalou, and W. Wiesbeck, "A stochastic spatial channel model based on wave-propagation modeling," *IEEE Journal on Selected Areas in Communications*, vol. 18, no. 1, pp. 6–15, 2000.

[19] M. Toeltsch, J. Laurila, K. Kalliola, A. F. Molisch, P. Vainikainen, and E. Bonek, "Statistical characterization of urban spatial radio channels," *IEEE Journal on Selected Areas in Communications*, vol. 20, no. 3, pp. 539–549, 2002.

[20] Z. Huang and X. Cheng, "A general 3D space-time-frequency non-stationary model for 6G channels," *IEEE Transactions on Wireless Communications*, vol. 20, no. 1, pp. 535–548, 2021.

[21] N. Czink, P. Cera, J. Salo, E. Bonek, J.-p. Nuutinen, and J. Ylitalo, "A framework for automatic clustering of parametric MIMO channel data including path powers," in *Proceedings of the IEEE Vehicular Technology Conference*, pp. 1–5, Montreal, QC, Canada, June 2006.

[22] N. Czink and C. Mecklenbrauker, "A novel automatic cluster tracking algorithm," in *Proceedings of the 2006 IEEE 17th International Symposium on Personal, Indoor and Mobile Radio Communications*, pp. 1–5, Helsinki, Finland, September 2006.

[23] X. Cai, G. Zhang, C. Zhang, W. Fan, J. Li, and G. F. Pedersen, "Dynamic Channel modeling for indoor millimeter-wave propagation channels based on measurements," *IEEE Transactions on Communications*, vol. 68, no. 9, pp. 5878–5891, 2020.

[24] J. H. Kim, Y. Yoon, and Y. J. Chong, "The distance characteristics of R.M.S. delay spread at urban low-rise environment," in *Proceedings of the 2016 International Conference on Information and Communication Technology Convergence (ICTC)*, pp. 1020–1022, Jeju, South Korea, October 2016.

[25] K. Mao, Q. Zhu, Y. Qiu et al., "A UAV-aided real-time channel sounder for highly dynamic nonstationary A2G scenarios," *IEEE Transactions on Instrumentation and Measurement*, vol. 72, pp. 1–15, 2023.

[26] G. Matz, "On non-WSSUS wireless fading channels," *IEEE Transactions on Wireless Communications*, vol. 4, no. 5, pp. 2465–2478, 2005.

[27] M. Herdin, N. Czink, H. Ozcelik, and E. Bonek, "Correlation matrix distance, a meaningful measure for evaluation of non-stationary MIMO channels," in *Proceedings of the 2005 IEEE 61st Vehicular Technology Conference*, pp. 136–140, Stockholm, Sweden, September 2005.

[28] B. Chen, Z. Zhong, and B. Ai, "Non-stationary channel characteristics in high-speed railway," in *Proceedings of the 2015 IEEE International Symposium on Antennas and Propagation USNC/URSI National Radio Science Meeting*, pp. 97-98, Vancouver, BC, Canada, July 2015.

[29] Q. Wang, D. W. Matolak, and B. Ai, "Shadowing characterization for 5-GHz vehicle-to-vehicle channels," *IEEE Transactions on Vehicular Technology*, vol. 67, no. 3, pp. 1855–1866, 2018.

[30] R. He, O. Renaudin, V.-M. Kolmonen et al., "Characterization of quasi-stationarity regions for vehicle-to-vehicle radio channels," *IEEE Transactions on Antennas and Propagation*, vol. 63, no. 5, pp. 2237–2251, 2015.

[31] A. Paier, T. Zemen, L. Bernado et al., "Non-WSSUS vehicular channel characterization in highway and urban scenarios at 5.2GHz using the local scattering function," in *Proceedings of the 2008 International ITG Workshop on Smart Antennas*, pp. 9–15, Darmstadt, Germany, February 2008.

[32] Y. Liu, L. Xiong, D. Fei, J. Du, Q. Wang, and C. Yan, "Characteristics for train-to-train channel based on ray tracing," in *Proceedings of the 2022 IEEE 8th International Conference on Computer and Communications (ICCC)*, pp. 47–51, Chengdu, China, December 2022.